

2

AD-A276 416



ADVANCED OPTICAL FIBER COMMUNICATION SYSTEMS

ONR Status Report for the period August 1, 1993 through March 1, 1994

R&T Project Code: 4148130-01

Grant Number: N00014-91-J-1857

Professor Leonid G. Kazovsky, Principal Investigator

Department of Electrical Engineering

Durand 202, MC-4055

Stanford University

Stanford, CA 94305-4055

DTIC
ELECTE
MAR 04 1994
S E D

ABSTRACT

Our research is focused on three major aspects of advanced optical fiber communication systems: dynamic wavelength division multiplexing (WDM) networks, fiber nonlinearities, and high dynamic range coherent analog optical links. In the area of WDM networks, we have designed and implemented two high-speed interface boards and measured their throughput and latency. Furthermore, we designed and constructed an experimental PSK/ASK transceiver that simultaneously transmits packet-switched ASK data and circuit-switched PSK data on the same optical carrier. In the area of fiber nonlinearities, we investigated the theoretical impact of modulation frequency on cross-phase modulation (XPM) in dispersive fibers. In the area of high dynamic range coherent analog optical links, we developed theoretical expressions for the RF power transfer ratio (or RF power gain) and the noise figure (NF) of angle-modulated links. We then compared the RF power gains and noise figures of these links to that of an intensity modulated direct detection (DD) link.

Approved for public release
Distribution

4088 94-06541





STAR LABORATORY • INFORMATION SYSTEMS LABORATORY

Department of Electrical Engineering, Stanford University, Stanford CA 94305-4055

Leonid G. Kazovsky
Professor of Electrical Engineering
Durand 202, MC-4055
Tel. (415) 725-3818
Fax (415) 723-9251
E-mail leonid@sierra.stanford.edu

Defense Technical Information Center
Building 5, Cameron Station
Alexandria, VA 22304-6145

February 23, 1994

Subject: Contract # N00014-91-J-1857 "Advanced Optical Fiber Communication Systems: Digital WDM Interconnects and Local Area Networks; Analog Signal Transport; Impact of Fiber Non-Linearities": Status Report.

Gentlemen:

Attached to this note please find our progress report for the above titled project. Should you have any questions, please do not hesitate to contact me at 415-725-3818.

Sincerely,

Leonid G. Kazovsky
Professor of Electrical Engineering

Encl.

ADN

1000 1000 1000

1. WDM Networks

Data-Link and Network Layers: STARNET, a broadband optical network, is intended to provide a wide variety of network services. Over a single physical passive star topology network, STARNET offers all users both a moderate-speed (125 Mbps) shared-channel packet-switched subnetwork and reconfigurable high-speed (up to 2.5 Gbps per node) circuit-switched subnetwork.

Fig. 1 shows how STARNET, through the combination of wavelength-division multiplexing and coherent optical reception, allows for two independent logical subnetworks to function over a single

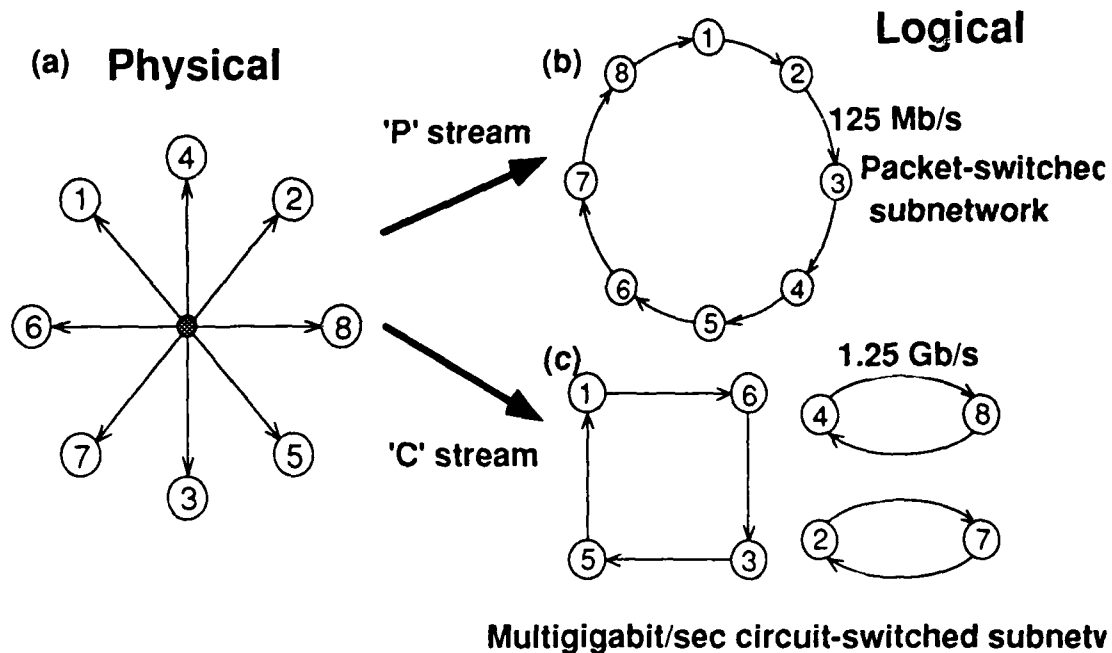


Figure 1. Through the use of WDM, STARNET maps a physical star topology (a) into both (b) a logical ring topology in the moderate-speed subnetwork and (c) a reconfigurable connection in the high-speed subnetwork.

Justification <i>plr</i>	
By <i>A261802</i>	
Distribution/	
Availability Codes	
Dist	Avail and/or Special
<i>A-1</i>	

physical passive star. The 125 Mbps subnetwork is configured by tuning each node's ASK receiver to the previous node's transmitter wavelength, thus forming a fixed logical ring topology (Fig. 1-b). The reconfigurable high-speed subnetwork nodes use their wavelength tunable PSK receiver to form point-to-point or variable ring connections (Fig. 1-c). The communication required to set up virtual circuits and to configure the high-speed sub-network is performed over the moderate-speed subnetwork.

The high-speed subnetwork is circuit-switched because the lasers used in the receivers tune slowly. Therefore, the configuration of the high-speed subnetwork is relatively long lasting. To provide topological flexibility in high-speed links, we have provided electronic packet-switching at each node while the topology remains circuit-switched.

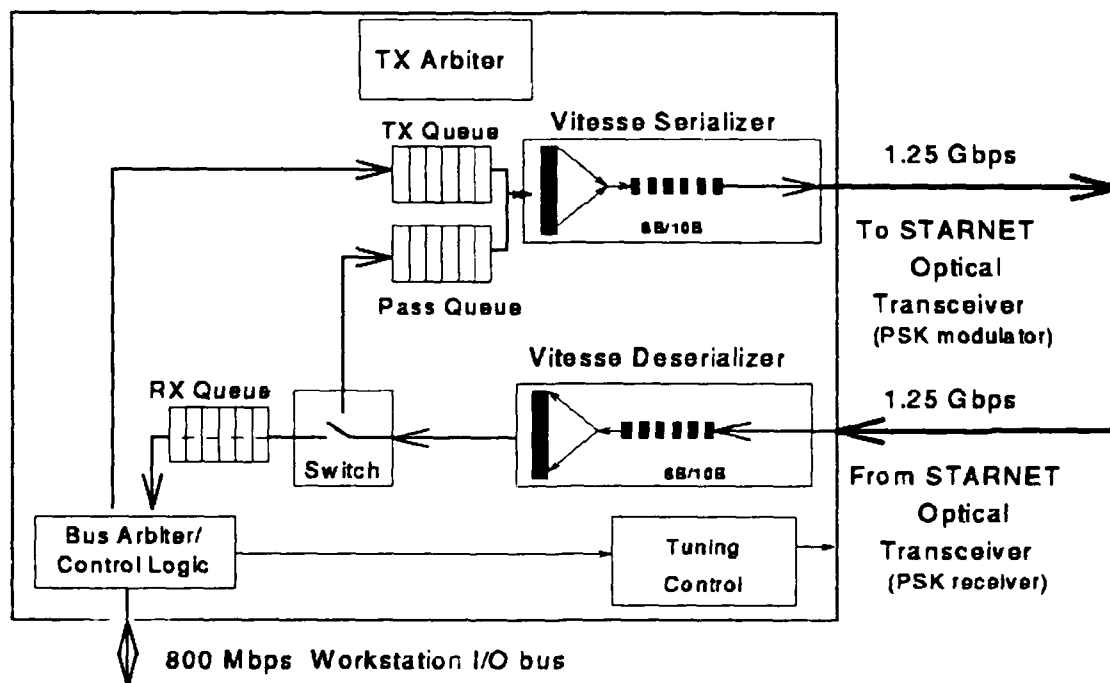


Figure 2. Block diagram of the high-speed subnetwork interface board.

In Fig. 2 we show a block diagram of an interface card which connects a DECstation 5000/240 to the STARNET high-speed subnetwork. The main elements are an I/O bus arbiter, an arbiter for the scheduling access to the high speed link, and a 2x2 switch which routes packets to the receive or pass queues. Three FIFOs provide for queuing of packets before they are transmitted over the network, received into host memory or retransmitted (passed) to the network. There are two bottlenecks associated with the high-speed subnetwork interface: first, the I/O bandwidth must be shared between the workstation's transmit and receive data streams; second, the output link must be shared between the workstation's transmit stream and pass-through traffic. In either case, the sum of the instantaneous input bit rates can exceed the maximum output bit rate. The interface must allocate bandwidth to minimize the probability of overflowing the queues while also remaining equitable when the network is congested.

The technique that we use to allocate bandwidth is shown on Fig. 3. A two-slot cycle is formed, and each of the time slots is allocated to one of the competing streams. By adjusting the time slot sizes, the interface dynamically modifies the bandwidth allocation depending upon actual demand.

We have measured the throughput and latency performance of the interface. The maximum sustained transmit-only throughput is 640 Mbps from the workstation to the network. The maximum sustained receive-only rate is 480 Mbps. The reason why we have higher transmit throughput than receive throughput is that in transmit, it takes 32 additional cycles to do one DMA operation which fetches 8 packets (128 cycles). On the other hand, in receive, it takes 13 additional cycles to fetch 1 packet (16 cycles). In normal network operation, these rates would be shared. To our knowledge, this is the fastest workstation-to-network throughput attained to date.

We have also performed simulations and experiments to measure the transmit latency of the interface. Fig. 4a shows the impact of burst size (average number of consecutive packets sent) on the transmit latency. In this figure, the average transmit bandwidth is 100 Mbps, and has been allocated up to 250 Mbps of the 1 Gbps total bandwidth. Nevertheless, because the transmit traffic is bursty, it can

exceed its allocation in the short term. The result is that the average latency increases as the burst size (instantaneous bandwidth) increases. Several experimentally measured transmit latency points are indicated in the figure.

Bandwidth Allocation in the High-Speed Subnetwork

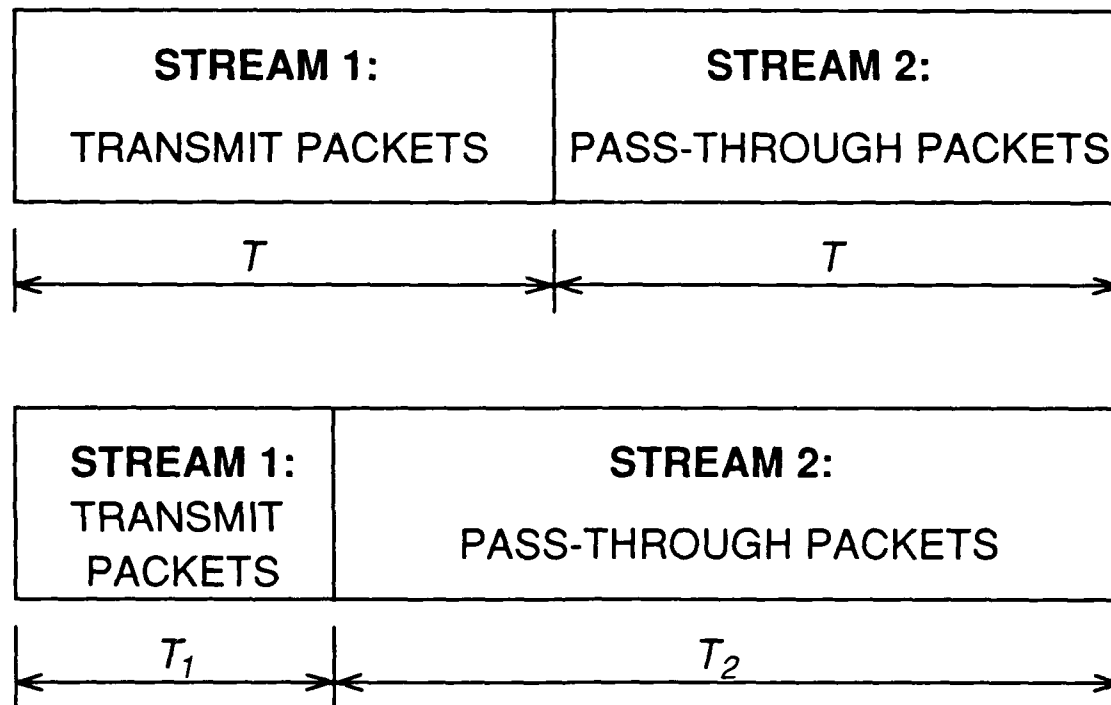
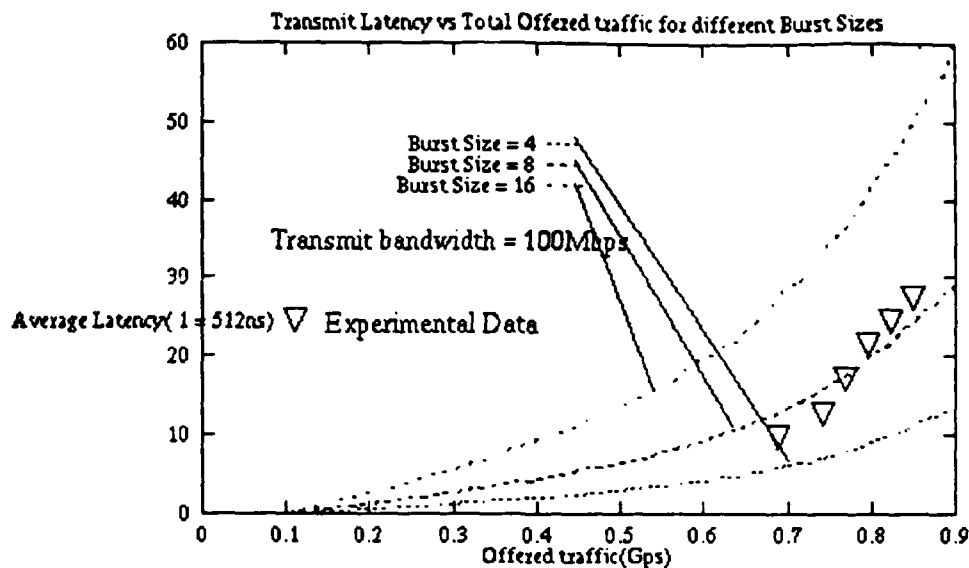
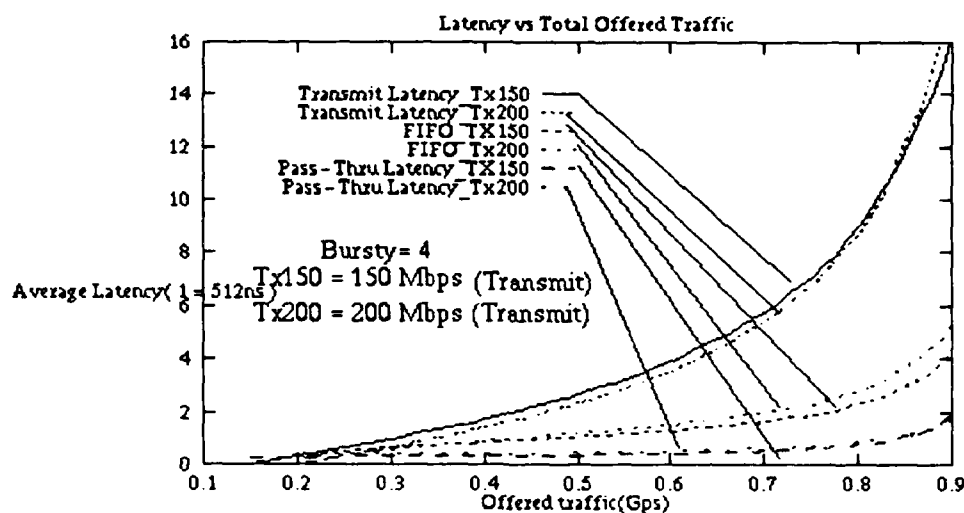


Figure 3. Dynamic bandwidth allocation in the high-speed network interface.

Fig. 4b shows the behavior of the transmit and pass-through latency as a function of total offered traffic. For low total offered traffic, the transmit latency is relatively unaffected by the occasional pass-through burst, while the pass-through traffic experiences some extra latency and the transmit traffic has



(a)



(b)

Figure 4. Latency performance of the high-speed interface: In (a), the latency of the transmit traffic increases as the burst size (instantaneously offered bandwidth) and the total offered traffic increase. In (b), the latency of the pass-through and transmit traffic is shown (for average transmit rates of 150 and 200 Mbps). The transmit latency increases as the average bandwidth increases. The pass-through traffic latency, however, remains relatively unaffected by the increased transmit bandwidth. Also plotted for comparison, is the latency of the unarbitrated FIFO approach.

arbitrated access to the network. The pass-through traffic latency, however, remains relatively unaffected by the increased transmit bandwidth. Also plotted for comparison is the latency of the unarbitrated FIFO approach. Note that although the transmit traffic 'pays' an initial latency penalty to gain admission to the network, the traffic sees reduced latency (in comparison to the unarbitrated approach) in each subsequent hop to its final destination. After a few hops, it is evident that the average total latency is less than that of the unarbitrated approach.

We constructed and debugged two STARNET node interfaces. These two interfaces are almost functional and ready to be interfaced with optics. A few software bugs still remain to be fixed. These two interfaces have been installed in two respective workstations. We are now able to communicate data between these two workstations over a copper wire, soon to be replaced with optics. Based upon performance analysis and latency measurements on the prototype, we decided to have deeper FIFOs to incorporate the burstiness of data. In these two new interfaces we have doubled the size of Receive FIFO. Transmit FIFO and Pass FIFO have remained the same size as before. The sizes of the FIFOs are as follows:

TX FIFO 512 words

RX FIFO 2048 words

PASS FIFO 2048 words

The reason we had to increase the receive FIFO was that its input channel is running at 1 Gbps, while its output link, the TURBO channel bus, is running at only 800 Mbps half duplex. Therefore, at certain instances, many packets can accumulate in the queue. If the queue is not big enough, significant packet loss can occur. To minimize the packet loss probability, we made the receive FIFO bigger. This is not the case for the TX FIFO and RX FIFO since both have output links that operate faster or at the same speed as the input links. The input link to the TX FIFO is the Turbo channel bus (800 Mbps half duplex), and the output link is optical fiber running at 1 Gbps. For the PASS FIFO, the input and output

are both running at 1 Gbps. In addition, we have a TX arbitrator chip that is 3 times bigger than the prototype board to fully implement the bandwidth scheme discussed earlier.

Optical Transceiver: We designed and constructed an experimental PSK/ASK transceiver for STARNET, a wavelength-division multiplexed computer communication network. The transceiver simultaneously transmits and receives 125 Mb/s FDDI-compatible, packet-switched, ASK data and 2.488 Gb/s circuit-switched PSK data on the same optical carrier. The transmitter uses an integrated phase and amplitude modulator and has an output power of 5 dBm at 1.32 μm . The 2.488 Gb/s PSK receiver has an integrated clock and data regenerator, and the 125 Mb/s ASK receiver has FDDI computer interfaces.

We found that both PSK data and ASK data can be transmitted simultaneously on the same optical carrier. However, the simultaneous use of amplitude and phase modulation on a single lightwave creates additional sensitivity penalties in both the ASK and PSK subsystems.

Fig. 5 shows the experimental setup used to demonstrate and to investigate simultaneous transmission and reception of ASK packet-switched and PSK circuit-switched data using the same optical carrier. The individual (not simultaneous) performance of the ASK and PSK transceivers has been reported in the previous progress report. Two workstations with FDDI interfaces measure the performance of the 125 Mb/s ASK link while the BER test set measures the BER of the 2.488 Gb/s PSK link. The ASK-FDDI ring was characterized using the FDDI link-error-event detection hardware and software.

The link error rate (LER) is a positive integer reported by the FDDI software; it is defined as:

$$\text{LER} = \text{INT} \left[\left\lceil \log \left(\frac{\text{estimated bit errors}}{\text{transmitted bits}} \right) \right\rceil \right] \quad (1-1)$$

Thus, a 2×10^{-10} error rate is reported as a LER of 9. Although the LER is roughly quantized, it nevertheless provides a reasonable measure of the link's performance.

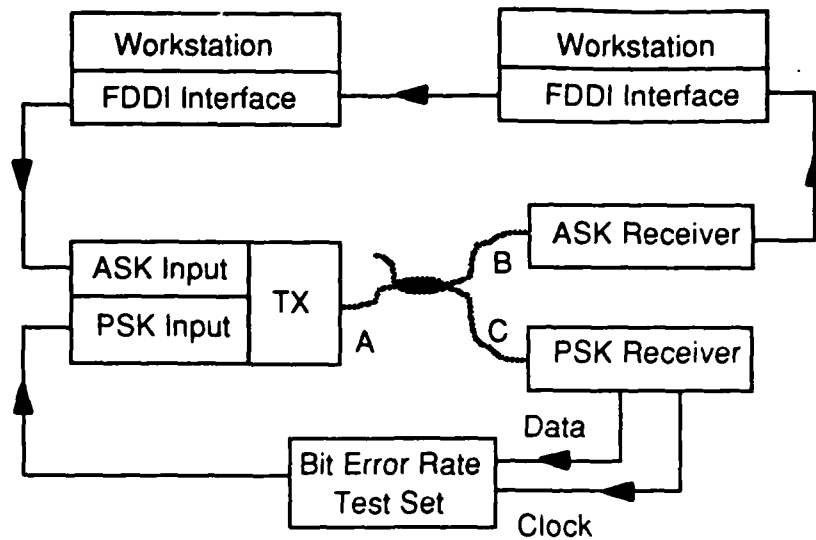


Figure 5. Block diagram of the experimental setup used to investigate the experimental STARNET transceiver.

We first characterized the performance of the ASK-FDDI ring without phase modulation of the lightwave. For an amplitude modulation depth $m = 100\%$, the ASK-FDDI ring operated with a LER of 9 for a peak received signal power of -41.3 dBm, measured at point B in Fig. 5. This is 3.7 dB greater than the received signal power required for a BER of 10^{-9} when a BER test set is used for characterization. The 3.7 dB penalty is due to the reduced performance of the FDDI interfaces compared to the BER test set.

Simultaneous amplitude and phase modulation of the transmitted signal causes additional errors in both the PSK and ASK receivers as shown in Fig. 6. The PSK receiver sensitivity is deteriorated by the amplitude modulation due to: (1) a reduction in received signal power when an ASK '0' bit is transmitted, and (2) amplitude modulation crosstalk in the optical phase-locked loop. The ASK receiver sensitivity is

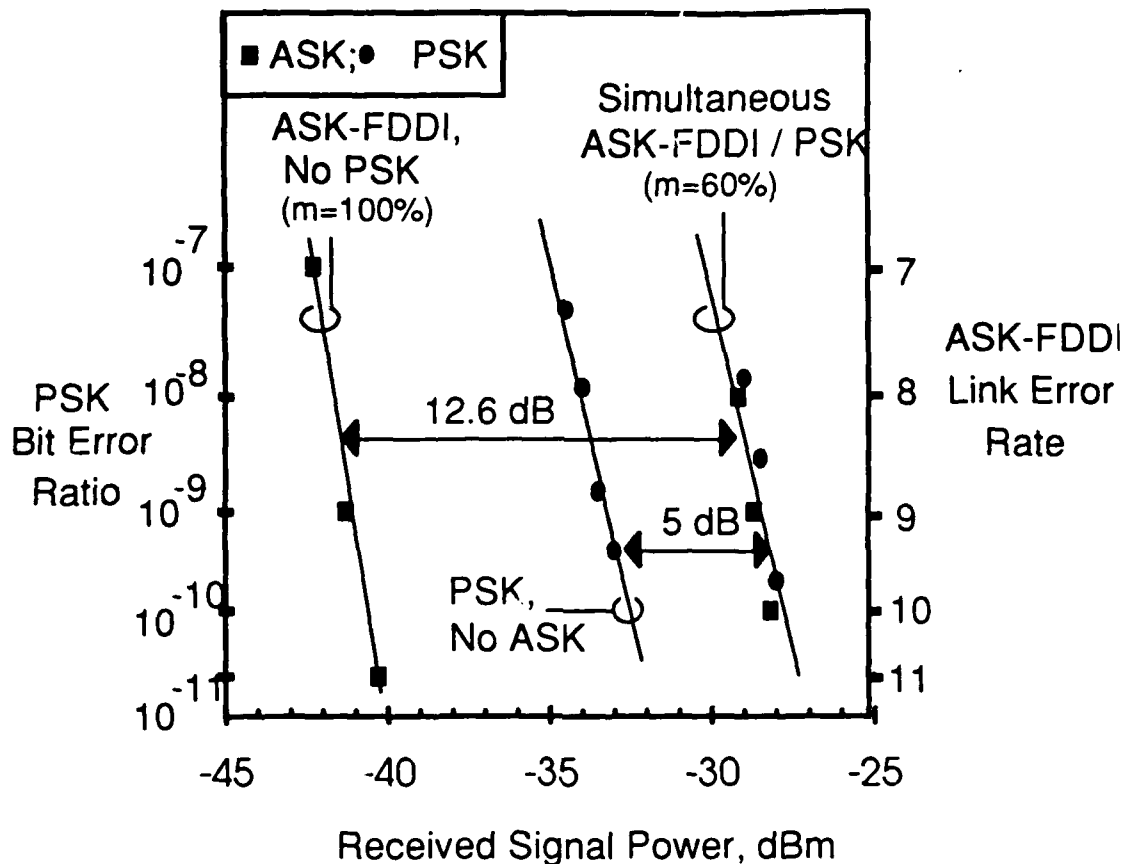


Figure 6. BER curves of ASK and PSK receivers operating simultaneously.

deteriorated by phase modulation due to non-ideal cancellation of phase fluctuations in the ASK receiver; this phenomenon is similar to phase-to-amplitude noise conversion.

The sensitivity of the ASK-FDDI receiver is -41.3 dBm when the modulation depth is 100%, and the PSK receiver sensitivity is -33.3 dBm when there is no ASK modulation. For optimum performance, the two receivers should have equal sensitivities. Therefore, we decreased the ASK modulation depth to a level where the ASK-FDDI receiver operates with a LER better than 9 and the PSK receiver operates with a BER less than 10^{-9} simultaneously. This occurs when the ASK modulation depth is adjusted to $m=60\%$. The resulting optimum receiver sensitivity is -25 dBm, measured at point A in Fig. 5. As shown in Fig. 6, the ASK modulation causes a 5 dB penalty to the PSK receiver, and the PSK modulation and

modulation depth adjustment cause a 12.6 dB penalty to the ASK FDDI receiver. Even with these penalties, the system power budget is 30 dB.

Table 1. Definitions and numerical values of the system parameters.

α	= 3 dB, Excess loss of the star coupler
B	= 2.5 GHz, Electrical bandwidth
B_o	Optical bandwidth
G	Optical gain
G_o	Unsaturated gain
$h\nu$	Photon energy
I_{th}	= 18 pA/Hz ^{1/2} , Thermal noise current
n_{sp}	= 5, Spontaneous emission noise factor
P	Received optical power
P_i	= 1 mW, Signal laser output power
P_{LO}	= 1 mW, LO laser output power
P_{sat}	= 10 mW, Local saturation power of the optical amplifier
q	Electronic charge
R	= 1.25 A/W, Responsivity of the photodetector
σ_{th}	Thermal noise of the receiver
σ_{sh}	Shot noise due to signal light and spontaneous emission
σ_{s-sp}	Beat noise between signal light and spontaneous emission
σ_{sp-sp}	Beat noise between spontaneous emission
σ_{LO-sp}	Beat noise between LO light and spontaneous emission

Amplifier Model: We investigated the use of optical amplifiers to expand the power budget limit of star networks using: (a) direct detection and (b) coherent detection (PSK). Our analysis considers both amplifier noise and gain saturation simultaneously. Our study focuses on the impact of amplifier noise and gain saturation of optical amplifiers on the power budget limit of star networks. As any amplifier, optical amplifiers add noise to the amplified signal. The definitions and values of the mathematical symbols used in this analysis are listed in Table 1. The spectral density of the amplified spontaneous emission (ASE) noise at the output of the amplifier is given by:

$$\eta_{sp} = n_{sp} (G - 1) h\nu \quad (1-2)$$

where n_{sp} is the spontaneous emission noise factor, G is the optical amplifier gain and $h\nu$ is the photon energy. The optical amplifier gain decreases when the incident optical power becomes comparable to the saturation power P_{sat} . The amplifier gain saturation is modeled by an equation that relates the amplifier gain G to the total input power P_{in} as:

$$P_{in} = \frac{P_{sat}}{G - 1} \ln \left(\frac{G_0}{G} \right) \quad (1-3)$$

For a star network, an amplifier is used in every arm. For simplicity, we assume no link attenuation and consider only the effect of the splitting and excess losses in the star coupler

In addition to thermal noise and shot noise, there are receiver noise contributions coming from the beating of ASE noise with the signal and itself. For the direct detection system, the receiver noise components are:

$$\begin{aligned} \sigma_{th}^2 &= I_{th}^2 B \\ \sigma_{sh}^2 &= 2qR(P + \eta_{sp} B_o) B \\ \sigma_{s-sp}^2 &= 4R^2 P \eta_{sp} B \end{aligned} \quad (4)$$

$$\sigma_{sp-sp}^2 = 2R^2 \eta_{sp}^2 (2B_o - B) B \quad (5)$$

For direct detection WDM systems, there are three possible positions for optical amplifiers: (1) at the transmitter (or anywhere before the star coupler); (2) after the star coupler but before the tunable optical filter (the optical filter is used to select the desired signal and to reject the ASE noise outside the signal bandwidth) and (3) after the optical filter.

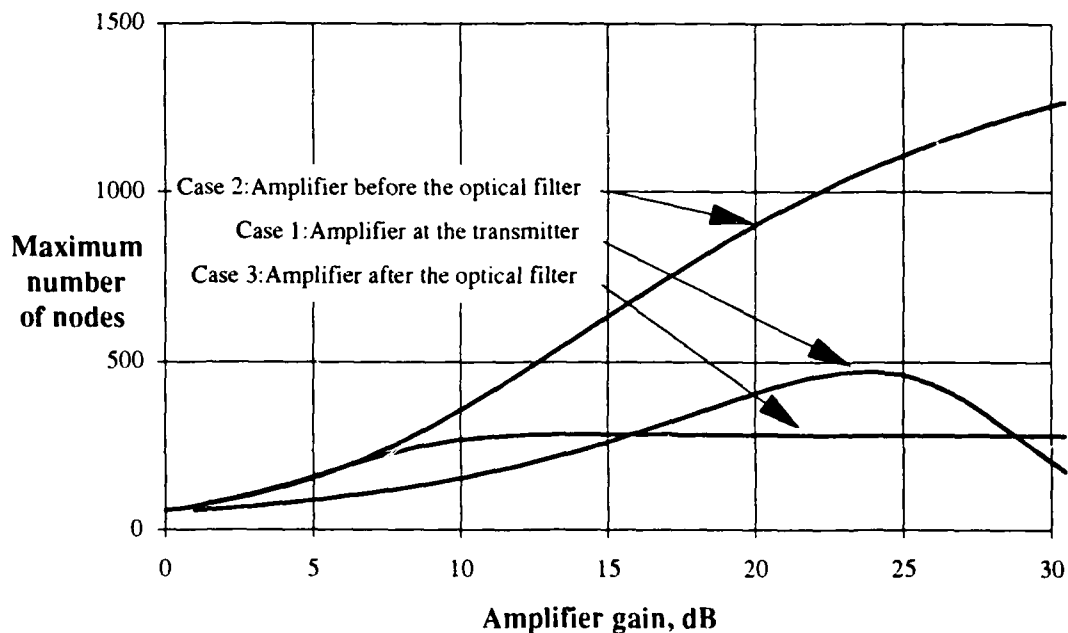


Figure 7. Maximum possible number of WDM nodes versus amplifier gain for direct detection star networks. The three positions for optical amplifiers are (1) at the transmitter; (2) before the optical filter (after the star coupler) and (3) after the optical filter.

First, we consider the optical signal power. The received signal power at the detector is the largest in case 3 because the amplifier gain experiences a lower degree of gain saturation than cases 1 and 2.

Next, we consider the noise power at the receiver. In case 1, the ASE noise from each amplifier is reduced by the coupler loss. However, the noise from other amplifiers is added to each output of the

coupler. The situation becomes worse when the other nodes are transmitting zeroes and generating large amounts of ASE noise because of the high unsaturated amplifier gain. In the following analysis, the worst case will be assumed. In cases 2 and 3, the ASE noise at the receiver is generated by only one amplifier. In case 3, since there is no optical filtering between the amplifier and the receiver, the entire ASE bandwidth of 4 THz is seen at the receiver leading to a large noise penalty. In case 2, the ASE noise is smaller since it is partially suppressed by the optical filter.

Fig. 7 shows the maximum theoretically possible number of nodes plotted against the amplifier gain for the three possible placements of optical amplifiers. The number of nodes that can be supported is determined by requiring that the bit error rate for any source and destination pair be smaller than a specific target, 10^{-9} in this report. For low amplifier gains, all three cases are limited by the thermal noise of the receiver. As the gain increases, the optical signal power increases and hence the number of nodes increases. At larger gains, the dominant noise components are the ASE beat noises, and the three cases behave quite differently. In case 1, the total ASE noise power increases in proportion to the unsaturated gain (because most of the ASE noise is due to amplifiers attached to other transmitters) while the received signal power increases in proportion to the saturated gain. Therefore, the system performance degrades at high gains. In cases 2 and 3, the ASE noise power is proportional to the saturated gain. In case 3, because of a wider ASE noise spectrum, the system performance becomes saturated with the spontaneous-spontaneous noise at a lower gain. Comparing the three cases, case 2 (amplifier before the optical filter) offers the best system performance.

In coherent systems, the main noise components are:

$$\begin{aligned}
 \sigma_{th}^2 &= I_{th}^2 B \\
 \sigma_{sh}^2 &= 2qR(P + P_{LO} + \eta_{sp} B_o)B \\
 \sigma_{LO-sp}^2 &= 4R^2 P_{LO} \eta_{sp} B
 \end{aligned}
 \tag{1-6}$$

The signal-spontaneous and spontaneous-spontaneous beat noises are common-mode components and, hence, can be suppressed by a balanced receiver.

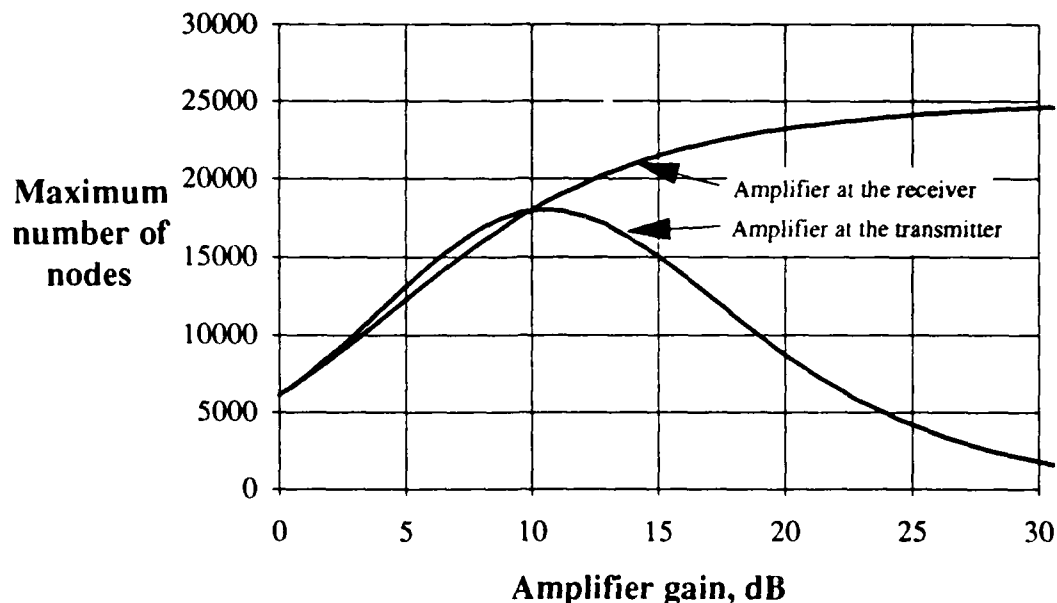


Figure 8. Maximum theoretically possible number of nodes versus amplifier gain for coherent star networks. The two positions for optical amplifiers are (1) at the transmitter and (2) at the receiver.

In coherent systems, the channel is selected by the IF filter in the receiver, and a tunable optical filter is not necessary. There are two positions to put the amplifiers: (1) at the transmitter (or anywhere before the star coupler) and (2) at the receiver (or anywhere after the star coupler).

Fig. 8 plots the maximum theoretically possible number of nodes against the amplifier gain for the two placements of optical amplifiers. The behavior is similar to that for direct detection. For low gains, the two cases are limited by the shot noise generated by the local oscillator (LO) laser, and the number of

nodes increases with the gain (since the LO shot noise is independent of the optical amplifier gain). In case 1, for gains larger than 10 dB, the system performance degrades with the gain because of the increasing ASE noise power. Comparing the two cases, case 2 (amplifier at the receiver) gives the best system performance.

To summarize, we have shown that optical amplifiers can be used to increase the limit imposed by the power budget on the scalability of a star network. In general, the best position for placement of optical amplifiers is (a) after the star coupler before the tunable optical filter for direct detection systems and (b) at the receiver for coherent systems.

2. IMPACT OF FIBER NONLINEARITIES ON OPTICAL COMMUNICATION SYSTEMS

THEORETICAL ANALYSIS OF XPM IN DISPERSIVE FIBERS: We investigated theoretically the impact of modulation frequency on cross-phase modulation (XPM) in dispersive fibers. XPM is the modulation of the phase of one optical wave by power fluctuations of another optical wave copropagating in the same fiber. XPM is particularly important in phase-sensitive lightwave systems. The impact of XPM on angle-modulated wavelength-division multiplexing (WDM) systems has been studied before for the case of near-zero group velocity dispersion (GVD). Conventional single-mode fiber is highly dispersive at

1.55 μm with the dispersion coefficient $D \gg 15 \text{ ps/nm}\cdot\text{km}$. In dispersive fibers, the group velocity mismatch among different wavelength channels can significantly influence the strength of XPM, depending on modulation frequency and wavelength separation. We found that the XPM index depends on fiber length, fiber chromatic dispersion, wavelength separation between the signal and the pump, and the intensity modulation frequency. At high modulation frequencies, the XPM index is inversely proportional to the product of the modulation frequency and wavelength separation. Part of the results have been submitted for publication to the *IEEE Photonics Technology Letters*.

XPM in a two-channel system with sinusoidal intensity modulation has been analyzed. We will show the influence of modulation frequency and wavelength separation on the XPM index.

Consider two optical waves with the same polarization copropagating in a single-mode optical fiber. Let $A_j(z, t)$ be the slowly-varying complex field envelope of each wave normalized to make $|A_j|^2$ equal to the instantaneous optical power. If channel 1 (probe) is CW and the intensity of channel 2 (pump) is sinusoidally modulated with angular frequency Ω_m , the expressions for the optical powers at $z=0$ are

$$P_1(0, t) = |A_1(0, t)|^2 = P_{10} . \quad (2-1)$$

$$P_2(0, t) = |A_2(0, t)|^2 = P_{20} + P_{2m} \cos(\Omega_m t) . \quad (2-2)$$

The phase of channel 1 (probe) light is modulated by the sinusoidal power fluctuation in channel 2 (pump). The expression for the complex envelope of channel 1 at distance L can be expressed as

$$A_1(L, t) = A_1(0, t - \frac{L}{v_{g1}}) \exp(-\alpha L/2) \exp(i\phi_1(L, t)) . \quad (2-3)$$

where

$$\phi_1(L, t) = \gamma_1 (P_{10} + 2P_{20}) L_{eff} + \Delta\phi \cos(\Omega_m(t - L/v_{g2}) + \varphi) , \quad (2-4)$$

is the phase shift caused by SPM and XPM, and $\Delta\phi$ is the XPM index given by

$$\Delta\phi = 2\gamma_1 P_{2m} \sqrt{\eta_{XPM}} L_{eff} : \quad (2-5)$$

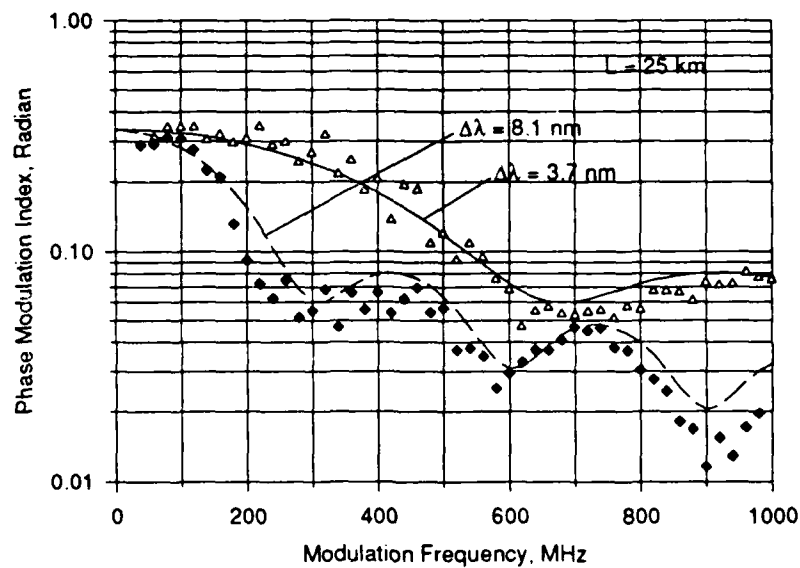


Figure 9. XPM index versus the modulation frequency of pump laser. Fiber length $L = 25$ km. The dots are experimental data, and the lines show the theoretical prediction.

L is the fiber length; $L_{eff} \equiv \frac{1 - e^{-\alpha L}}{\alpha}$ is the effective fiber length; η_{XPM} is the XPM efficiency given by

$$\eta_{XPM} \equiv \frac{\alpha^2}{\Omega_m^2 d_{12}^2 + \alpha^2} \left[1 + \frac{4 \sin^2(\Omega_m d_{12} L/2) e^{-\alpha L}}{(1 - e^{-\alpha L})^2} \right]; \quad (2-6)$$

and $d_{12} \equiv \frac{1}{v_{g1}} - \frac{1}{v_{g2}}$ is the walk-off parameter. In a non-zero dispersion region, $d_{12} \approx D\Delta\lambda_{12}$, where D is the dispersion coefficient and $\Delta\lambda_{12}$ is the wavelength separation between the two channels. $\Delta\phi$ can be approximated by

$$\Delta\phi \approx 2\gamma_1 P_{2m} \alpha L_{eff} / \Omega_m D \Delta\lambda_{12} \quad (2-7)$$

when $|\Omega_m d_{12}| \gg \alpha$ and $\alpha L \gg 1$.

Expressions (4)-(7) show that the phase of the probe light is modulated at Ω_m . The strength of this phase modulation depends on γ_1 , P_{2m} , L_{eff} , and η_{XPM} . In turn, η_{XPM} given by (6) depends on D , $\Delta\lambda$, and Ω_m . Numerical values of $\Delta\phi$ for our experiments are shown in Fig. 9. In general, at low modulation frequencies, the walk-off time $T_w \equiv |L/v_{g1} - L/v_{g2}|$ is much less than the period $T_0 \equiv 2\pi/\Omega_m$ of the pump modulation so that the portion of the probe light that propagates along the higher pump intensity experiences a larger refractive index throughout its propagation. Consequently, the resulting phase shift is larger than the phase shift on the probe light that propagates along the lower pump intensity. At higher modulation frequencies, $T_w \geq T_0$ so that each portion of the probe light experiences several cycles of pump intensity fluctuation. Therefore, the phase variation among different time segments of the probe light is small. At high frequencies, $\Delta\phi$ is approximately proportional to $(\Omega_m \Delta\lambda)^{-1}$.

We have shown theoretically that the cross-phase modulation (XPM) index depends on fiber length, fiber chromatic dispersion, wavelength separation, and the frequency of power fluctuation. A simple expression [5] for the XPM index has been derived and has been shown to agree well with experimental measurements. The results show that at high modulation frequencies, the XPM index is approximately inversely proportional to the product of the modulation frequency and wavelength separation. These results indicate that the XPM is expected to be smaller in communication systems operating at higher data rates and with larger wavelength separations.

3. COHERENT ANALOG LINKS

Angle-Modulated Link Theory: We found theoretical expressions for the RF power transfer ratio (or RF power gain) and the noise figure (NF) of the angle-modulated links which we have previously analyzed, including (a) a coherent FM link using direct modulation; (b) a coherent FM link using external modulation; (c) a coherent PM link using external modulation; (d) the heterodyne interferometric phase modulated (HIPM) link; and (e) the homodyne interferometric phase modulated (HPM) link. We compared the RF power gains and NFs of these links to that of an intensity-modulated direct detection (DD) link. We found that the RF losses in microwave integration and frequency or phase discrimination cause the RF gains (for realistic parameter values) of angle-modulated links to be lower than that of the direct detection link for optical powers greater than about -20 dBm. These RF losses also cause the noise figures of angle-modulated links to be higher than that of the direct detection link for optical powers greater than -20 dBm except in the case of external phase modulation. To compensate for this, low-noise amplification is required before integration and discrimination in angle-modulated links.

The RF power transfer ratio, or RF power gain G , of the link is defined as the ratio of the power delivered at the link output to the power available from the source.

$$G = \frac{S_o}{S_i} \quad (3-1)$$

It is easily obtained by measuring the input and output signal power levels and finding their ratio according to the above equation.

In general, RF amplifiers can be added before and after the optical link (as shown in Figure 10).

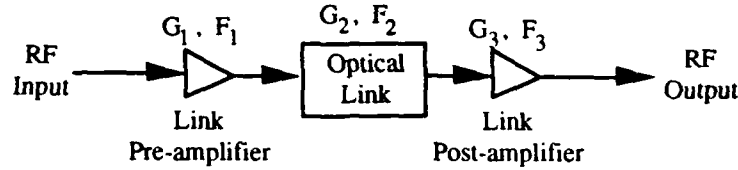


Figure 10. Optical link with a pre-amplifier and a post-amplifier.

The overall gain G of this amplifier- optical link - amplifier system is given by:

$$G = G_{in} G_{opt} G_{out} \quad (3-2)$$

where G_{opt} is the optical link gain, and G_{in} and G_{out} are the gains due to preamplification and postamplification, respectively. G_{opt} is determined by the electrical to optical and optical to electrical conversion efficiencies of optical components and the conversion losses of microwave components in the link. G_{opt} for the externally modulated direct detection link is given by:

$$G_{opt,DD} = \left(\frac{\pi}{2V_{\pi}} \right)^2 (rP_s)^2 R_s^2 \quad (3-3)$$

where R_s is the source impedance, r is the photodetector responsivity, P_s is the received optical power, P_{LO} is the local oscillator power, and V_{π} is the voltage required to generate a modulator phase shift of π . The value of $G_{opt,DD}$ is dependent on the choice of modulator operating point; in this case the operating point is chosen at the half-power point of the sinusoidal modulator characteristic.

Noise figure measures the degradation in the signal-to-noise ratio (SNR) between the input and output of a link and is defined as:

$$F = \frac{\frac{S_i}{N_i}}{\frac{S_o}{N_o}} = \frac{N_o}{GN_i} \quad (3-4)$$

where S_i and N_i are the input signal and noise powers, and S_o and N_o are the output signal and noise powers. By definition, the input noise power is the noise power from a matched resistor, $N_i = kTB$, where k is Boltzmann's constant, T is the resistor temperature, and B is the signal bandwidth. The output noise power can be expressed by:

$$N_o = GN_i + \eta B \quad (3-5)$$

where ηB is the additive noise introduced in the device or link. Substituting $N_i = kTB$, we can express the noise figure as:

$$F = 1 + \frac{\eta}{GkT} \quad (3-6)$$

For the direct detection optical link, the noise figure is

$$F_{DD} = 1 + \frac{\eta_{DD}}{G_{DD}kT} \quad (3-7)$$

where

$$\eta_{DD} = R_s \left[\frac{r^2 P_s^2}{4} 10^{\frac{RIN}{10}} + 2qrP_s + \frac{4kT}{R_s} \right] \quad (3-8)$$

The total noise figure for the system shown in Figure 10 can be determined using the following expression:

$$F = F_{in} + \frac{F_{opt}-1}{G_{in}} + \frac{F_{out}-1}{G_{in}G_{opt}} \quad (3-9)$$

For the case of optical links $G_{in}G_{opt} \ll 1$ so that

$$F \approx \frac{F_{out}-1}{G_{in}G_{opt}} \quad (3-10)$$

Expressing the terms in dB,

$$F \approx F'_{out} - G_{in} - G_{opt} = F'_{out} - G + G_{out} \quad (3-11)$$

This means that the noise figure can be minimized (a) using a high gain pre-amplifier G_{in} and (b) increasing the optical power (corresponds to increasing G_{opt}). The sum of the noise figure and RF transfer ratio for the optical link is constant:

$$F + G \approx F'_{out} + G_{out} = \text{constant} \quad (3-12)$$

Therefore, it is possible to construct a system having both desirable features of high gain and low noise figure.

A detailed derivation of the RF power gain for an externally modulated coherent FM link is given in this section. Results for the directly modulated coherent FM link, the externally modulated coherent PM link, the heterodyne interferometric PM (HIPM) link, and the homodyne interferometric PM (HPM) link are also given. The RF power gains which we present in this section correspond to the gain G_{opt} of the optical link section in Figure 10, which does not include the impact of pre/post-amplification. G_{opt} , therefore, represents a measure of the losses from imperfect electrical to optical and optical to electrical conversion efficiencies of optical components and the conversion losses of microwave components in the link.

A block diagram of an externally modulated coherent FM link is shown in Figure 11. The input voltage is of the form $V(t) = Vx(t)$, where $x(t)$ is a dimensionless time-varying signal. The integrator, for simplicity, is assumed to be an RC low pass filter with a voltage transfer characteristic

$$\frac{V_{out}(\omega)}{V_{in}(\omega)} = \frac{1}{1 + j\omega RC} \quad (3-13)$$

This filter serves as a good integrator for signals composed of frequencies far from baseband, such that $\omega RC \gg 1$, which is usually the case for frequencies on the order of a gigahertz. It can also be built very easily in microstrip or with lumped elements. If $V_{in}(t) = V(t)$, then

$$V_{out}(t) \approx \frac{V}{RC} \int_{-\infty}^t x(\tau) d\tau \quad (3-14)$$

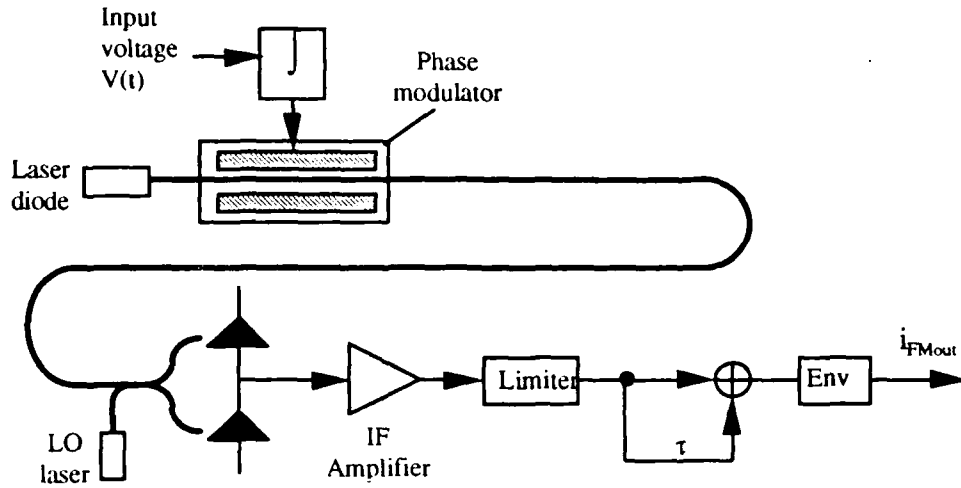


Figure 11. Externally modulated coherent FM link.

Assuming that a π phase shift is obtained from the modulator with a drive voltage V_π , the modulator output is

$$\sqrt{P_T} \exp \left[j \left(\omega_{op} t + \frac{\pi V}{V_\pi RC} \int_{-\infty}^t x(\tau) d\tau + \phi_{ns}(t) \right) \right] \quad (3-15)$$

where P_T is the optical power at the modulator output. Assuming that the photodetectors are well-matched, the output current is

$$i_{FMout}(t) \equiv \frac{1}{4f_{IF}} \left[\sqrt{P_s P_{LO}} \left[\omega_v x(t) - \frac{\omega_v^3}{6} \left(\frac{1}{4f_{IF}} \right)^2 x^3(t) \right] + 2r \sqrt{P_s P_{LO}} [\phi'_{ns}(t) - \phi'_{nLO}(t)] + n'_{D_{bp}}(t) \right] \quad (3-16)$$

where P_S is the normalized transmitted signal optical power*, ϕ_m is the phase noise of the signal laser, f_r is the receiver intermediate frequency, and ω_Δ is the frequency deviation. In this case, P_{LO} is the total received local oscillator power at the photodetector and $\phi_{nLO}(t)$ is the phase noise of the LO laser. n_{out} is the receiver output noise process.

Assuming that the link input and output are impedance-matched with resistance R_s and that the input signal $x(t)=\cos(\omega t)$, the output RF power S_o is easily found to be

$$\left(\frac{1}{4f_{IF}}\right)^2 2r^2 P_S P_{LO} \left(\frac{\pi V}{V_\pi RC}\right)^2 R_s L_{nl} \quad (3-17)$$

L_{nl} is the loss of RF signal power due to the generation of nonlinearities in the limiter and the envelope detector. The RF power transfer ratio is

$$G_{opt(Ext FM)} = \frac{S_o}{S_i} = \left(\frac{1}{4f_{IF}}\right)^2 4r^2 P_S P_{LO} \left(\frac{\pi}{V_\pi RC}\right)^2 R_s^2 L_{nl} \quad (3-18)$$

The RF power transfer ratios for the other angle-modulated links were derived in a similar manner. For the externally modulated coherent PM link, the RF gain is

$$G_{opt(Ext PM)} = \left(\frac{1}{4f_{IF}}\right)^2 4r^2 P_S P_{LO} \left(\frac{\pi}{V_\pi RC}\right)^2 R_s^2 L_{nl} \quad (3-19)$$

* The normalized transmitted signal optical power P_s is defined as follows. The received optical power $P_r = P_s L_n$ is the product of P_s and the intrinsic loss of the external modulator. In the case of direct frequency modulation or external angle modulation, the intrinsic loss factor is equal to 1. For the HIPM link and the HPM link, the intrinsic loss factor assumes the values 0.33 and 0.5, respectively.

which is identical to that of the externally modulated coherent FM link.

For the directly modulated coherent FM link, the RF gain is

$$G_{\text{opt (dir. FM)}} = \left(\frac{\pi \gamma}{2 f_{\text{IF}}} \right)^2 4 r^2 P_s P_{\text{LO}} L_{\text{nl}} \quad (3-20)$$

where γ is the FM response of the transmitter laser diode in GHz/mA.

For the HIPM link, the RF gain is

$$G_{\text{opt (HIPM)}} = \left(\frac{1}{4 f_{\text{IF}}} \right)^2 \frac{16}{81} r^2 P_s^2 J_1^2(\beta) \left(\frac{\pi}{V_{\pi} RC} \right)^2 R_s^2 L_{\text{nl}} \quad (3-21)$$

This RF gain is in terms of the signal input power only; it does not include the two supplemental sinusoidal modulator inputs required for the HIPM link. β is a function of the amplitudes of the two sinusoidal modulator inputs.

For the HPM link, the RF gain is

$$G_{\text{opt (HPM)}} = \left(\frac{1}{4 f_{\text{IF}}} \right)^2 \frac{1}{16} r^2 P_s^2 \left(\frac{\pi}{V_{\pi} RC} \right)^2 R_s^2 L_{\text{nl}} \alpha \quad (3-22)$$

α is the conversion loss (on the order of 6 dB) of the microwave mixers required in the receiver of the HPM link.

In angle-modulated links, the noise at the link output is not always of the form ηB in Equation (5) due to the nonlinear discrimination process. However, the derivation of noise figure is still straightforward using the formula

$$F_{(link)} = 1 + \frac{\text{noise power at link output}}{G_{(link)} kTB} \quad (3-23)$$

We give the output noise powers for the five angle-modulated links for which we derived the RF power transfer ratios. The noise figure is then obtained directly from (23). The noise power at the output of the externally modulated coherent FM link is

$$\eta_{(ext FM)} = R_s \left(\frac{1}{4 f_{IF}} \right)^2 \left[4r^2 P_s P_{LO} [4\pi \Delta\nu B] + \frac{(2\pi)^2}{3} \left(4qr(P_s + P_{LO}) + \frac{4kT}{R_s} \right) (f_{max}^3 - f_{min}^3) \right] \quad (3-24)$$

where $\Delta\nu$ is the laser linewidth, B is the signal bandwidth, q is the electron charge, and f_{min} and f_{max} are the minimum and maximum frequencies in the signal band, respectively.

The noise power at the output of the directly modulated coherent FM link is

$$\eta_{(dir FM)} = R_s \left(\frac{1}{4 f_{IF}} \right)^2 \left[4r^2 P_s P_{LO} [4\pi \Delta\nu B] + \frac{(2\pi)^2}{3} \left(4qr(P_s + P_{LO}) + \frac{4kT}{R_s} \right) (f_{max}^3 - f_{min}^3) \right] \quad (3-25)$$

which is identical to the output noise power for the externally modulated coherent FM link.

The noise power at the output of the externally modulated coherent PM link is

$$\eta_{(ext PM)} = R_s \left(\frac{1}{4 f_{IF} RC} \right)^2 \left[4r^2 P_s P_{LO} \left[\frac{\Delta\nu}{\pi} \left(\frac{1}{f_{min}} - \frac{1}{f_{max}} \right) \right] + \left(4qr(P_s + P_{LO}) + \frac{4kT}{R_s} \right) B \right] \quad (3-26)$$

The noise power at the output of the HIPM link is

$$\eta_{(\text{HIPM})} = R_s \left[\eta_{Dq} + r^2 P_s^2 \left(1 + \frac{2}{3} J_0(\beta) \right)^2 \eta_{Rq} \right] \left(\frac{1}{4 f_{IF} RC} \right)^2 \quad (3-27)$$

where η_{Dq} and η_{Rq} represent the power spectral densities of receiver noise and relative intensity noise at the HIPM link output, respectively.

The noise power at the output of the HPM link is

$$\eta_{(\text{HPM})} = R_s \alpha \left[2\eta_{Dq} + \frac{r^2 P_s^2}{2} 10^{\frac{RIN}{10}} B \right] \left(\frac{1}{4 f_{IF} RC} \right)^2 \quad (3-28)$$

Table 2 shows the values of relevant parameters which were used in the numerical computation of link RF power transfer ratios and noise figures versus normalized transmitted signal optical power. The parameters were chosen to be representative of realistic system components.

Parameter	Assumed Value	Parameter	Assumed Value
LO power P_{Lo}	10 mW	Mod. voltage V_π	15 V
RIN	-155 dB/Hz	HIPM index β	1
Relaxation osc. freq.	2 GHz	RC time constant	1.21E-9 s
Laser linewidth $\Delta\nu$	10 kHz or 1 MHz	Source impd. R_s	50 Ω
Signal bandwidth B	1 GHz	Conversion loss α	6 dB
Min. sig. freq. f_{min}	1 GHz	Nonlinear loss L_{nl}	6 dB
Max. sig. freq. f_{max}	2 GHz	Int. freq. f_{IF}	10 GHz
Laser FM resp. γ	1 GHz/mA	Responsivity r	0.8

Table 2-. Parameter values used in numerical computation of RF power transfer ratios and noise figures.

The RF power transfer ratios of the angle-modulated links are compared to that of the direct detection link in Fig. 12; these RF gains measure the efficiency of the links without any amplification.

At an optical power of -20 dBm, the coherent angle-modulated links and the direct detection link have approximately the same RF gain, with the externally modulated coherent links having an advantage of about 2 dB. As the optical power increases beyond 0 dBm, the RF gain of the direct detection link is upwards of 20 dB larger than that of the coherent links. The RF gains of the coherent links increase relative to that of the direct detection link as optical power decreases because coherent links remain much closer to the shot noise limit. All of the angle-modulated links have lower RF gains than the direct detection link because there are considerable RF losses due to the integrator and due to the microwave frequency discriminator. This means that extra amplification may be required in angle-modulated links before the integrator and the discriminator. The values of the RF gains are device dependent; for example, the RF gain of the directly modulated coherent FM link is proportional to the square of the laser FM response. Thus, device characteristics also have a significant impact on system RF gain.

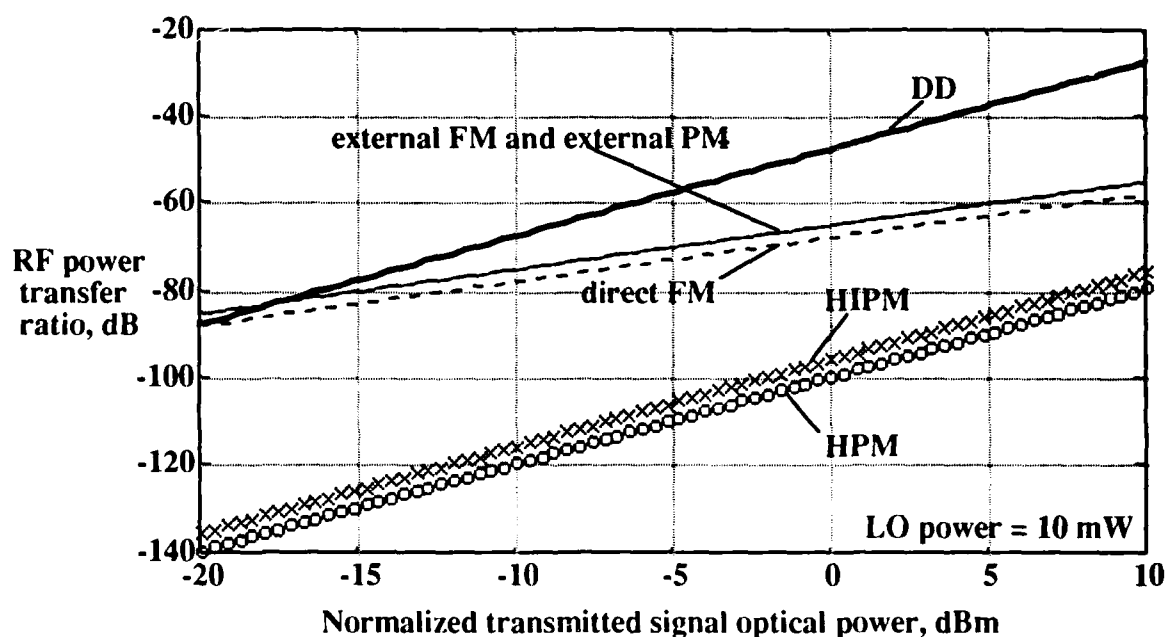


Figure 12. RF power transfer ratios (versus normalized transmitted signal optical power) of the angle-modulated links compared to that of the direct detection link.

The noise figures of the coherent angle-modulated links are compared to that of the direct detection link in Fig. 13. The curves are not straight due to the different power dependences of the

different noises which contribute. The thin solid lines show the noise figure of the coherent links for a low-linewidth laser such as an Nd:YAG. The dotted lines show the noise figure of the coherent links for a low-linewidth semiconductor laser such as a multi-quantum well (MQW) distributed feedback laser. The noise figures of the FM links are consistently higher than that of the DD links for optical powers from -18 dBm up, even for the low-linewidth laser. This is due to the low RF gains of these links and to the effect of frequency discrimination on white Gaussian noise. The noise figures of the PM links are approximately 20 dB lower than those of the FM links because phase discrimination does not change the white Gaussian character of the noise. The noise figure of the coherent angle-modulated links can be significantly improved through the use of low-noise amplifiers before integration and discrimination.

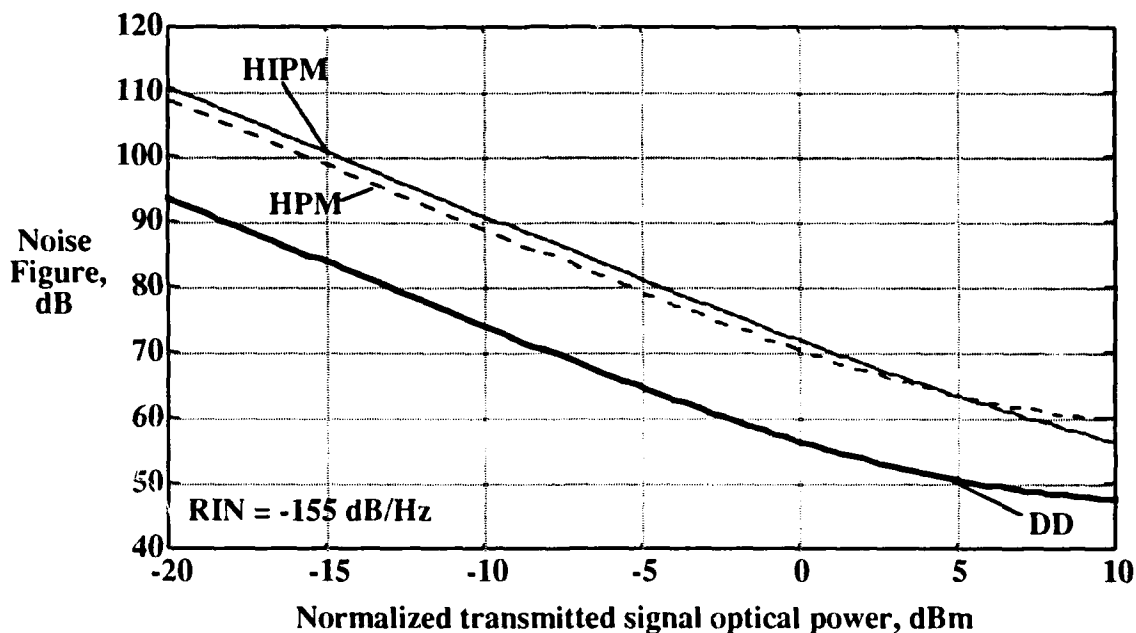


Figure 13. NF of the HIPM, HPM and DD links

Fig. 13 shows the noise figures of the HIPM and HPM links compared to that of the direct detection link for a laser relative intensity noise (RIN) power density of -155 dB/Hz. The noise figure of the direct detection link is approximately 15 dB lower than those of the interferometric links for optical

powers below 0 dBm. For larger optical powers, laser RIN begins to dominate, causing the difference in the noise figures to decrease. Similar to the coherent links, the high noise figures of the interferometric links are due to their low RF gains, which means that low-noise amplification is required before integration and discrimination. The noise figures are also dependent on the laser RIN; for a larger RIN, the noise figures of the interferometric links will decrease significantly relative to that of the direct detection link.

The main conclusions of our study of the RF power transfer ratio and the noise figure of angle-modulated links are (1) the RF losses in microwave integration and frequency or phase discrimination cause the RF gains (for realistic parameter values) of angle-modulated links to be lower than that of the direct detection link for optical powers greater than about -20 dBm; (2) these RF losses also cause the noise figures of angle-modulated links to be higher than that of the direct detection link for optical powers greater than -20 dBm except in the case of external phase modulation; (3) to compensate for this, low-noise amplification is required before integration and discrimination in angle-modulated links.

References

- [1] D. M. Pozar, Microwave Engineering, Addison-Wesley, N. Y., 1990, pp. 589-594.
- [2] R. F. Kalman, J. C. Fan, and L. G. Kazovsky, "Dynamic Range of Coherent Analog Fiber-Optic Links," *IEEE/OSA Journal of Lightwave Technology*, accepted for publication.
- [3] R. F. Kalman, J. C. Fan, and L. G. Kazovsky, "A Novel Analog Optical Link with High Dynamic Range," *IEEE Photonics Technology Letters*, vol. 5, no. 6, pp. 725-728, 1993.

Conclusions: In this report, we presented the progress of our group in three areas, namely: dynamic WDM networks, high dynamic range coherent optical analog links, and fiber nonlinearities. To summarize, in the area of WDM networks, we have implemented an optical transceiver which consists of a PSK transceiver and an ASK transceiver. Simultaneous transmission of 125 Mb/s FDDI-compatible, packet-switched, ASK data and 2.488 Gb/s circuit-switched, PSK data on the same optical carrier has been demonstrated. We have also designed and implemented two interface boards. The boards are now almost functional and ready to be interfaced with optics. Their throughput and latency have been measured. The results indicated that their performance varies in different traffic conditions. Furthermore, we have shown that optical amplifiers can be used to increase the limit imposed by the power budget on the scalability of a star network. In the area of fiber nonlinearities, we found that at high modulation frequencies the XPM index is approximately inversely proportional to the product of the modulation frequency and wavelength separation between the signal and pump. In the area of coherent analog links, we studied the RF power transfer ratio and noise figure of angle-modulated links. The results indicated that the RF losses in microwave integration and frequency, or phase, discrimination cause the RF gains of angle-modulated links to be lower than that of the direct detection link. These RF losses also cause the noise figure of angle modulated links to be higher than that of the direct detection link for optical powers greater than -20dBm except in the case of external phase modulation. To compensate for this, low-noise amplification is required before integration and discrimination in angle-modulated links.

List of publications between September 1, 1993 to March 1, 1994

I. Papers in Refereed Journals:

1. T. K. Chiang, N. Kagi, T. K. Fong, M. E. Marhic, L. G. Kazovsky, "Cross-Phase Modulation in Dispersive Fibers: Theoretical and Experimental Investigation of the Impact of Modulation Frequency," *IEEE/OSA Journal of Lightwave Technology*, submitted for publication.
2. D. J. M. Sabido IX, M. Tabara, T. K. Fong, R. F. Kalman, L. G. Kazovsky, "Experimental Linewidth-Insensitive Coherent Analog Optical Link," *IEEE/OSA Journal of Lightwave Technology*, submitted for publication.
3. N. L. Taranenko, L. G. Kazovsky, Y. N. Taranenko, "Three-Wave Envelope Solitons: Possibility of Controlling the Speed of Light in the Fiber," *IEEE/OSA Journal of Lightwave Technology*, submitted for publication.
4. O. K. Tonguz, M. O. Tanrikulu, L. G. Kazovsky, "Performance of Coherent ASK Lightwave Systems with Finite Intermediate Frequency," *IEEE Transactions on Communications*, submitted for publication.
5. T. K. Fong, D. J. M. Sabido IX, R. F. Kalman, M. Tabara, L. G. Kazovsky, "Linewidth-insensitive Coherent AM Optical Links: Design, Performance and Potential Applications," *IEEE/OSA Journal of Lightwave Technology*, accepted for publication.

6. T. K. Fong, M. Tabara, D. J. M. Sabido IX, L. G. Kazovsky, "Dynamic Range of Externally Modulated Analog Optical Links: Optical Amplification Versus Coherent Detection," *IEEE Photonics Technology Letters*, accepted for publication.
7. M. Hickey, L. G. Kazovsky, "The STARNET Coherent WDM Computer Communications Network: Experimental Transceiver Employing a Novel Modulation Format," *IEEE/OSA J. of Lightwave Technology*, accepted for publication.
8. R. F. Kalman, J. C. Fan, L. G. Kazovsky, "A Novel Analog Optical Link with High Dynamic Range," *IEEE Photonics Technology Letters*, accepted for publication.
9. T. K. Fong, D. J. M. Sabido IX, M. Tabara, L. G. Kazovsky, "Spurious-free Dynamic Range of Linewidth-insensitive Coherent AM Analog Optical Links," *IEE Electronics Letters*, Vol. 29, No. 23, November 11, 1993, pp. 2060-2061.

II. Conference Papers:

1. C. Barry, C. Noronha, N. Taranenko, S. Agrawal, L. G. Kazovsky, "Gigabit/s Optical Interface for WDM STARNET Network," OFC '94, February 1994.
2. D. J. M. Sabido IX, M. Tabara, T. K. Fong, L. G. Kazovsky, "Experimental Investigation of the Impact of EDFA's on Coherent AM Analog Optical Link," OFC '94, February 1994.
3. C. Barry, M. Hickey, C. Noronha, N. Taranenko, L. G. Kazovsky, "A Multi-Gbit/s Optical LAN Utilizing a WDM Star: Towards an Experimental Prototype," SPIE's OE/LASE '94, Los Angeles, CA, January 1994.
4. T. K. Fong, M. Tabara, D. J. M. Sabido IX, L. G. Kazovsky, "Dynamic Range of Analog Optical Links Using Optical Preamplifiers," SPIE's OE/LASE '94, Los Angeles, CA, January 1994.
5. L. G. Kazovsky, M. Hickey, "Toward Implementation of MultiGb/sec Optical Networks," Invited paper, IEEE LEOS Annual Meeting, San Jose, CA, November 1993.